Pressure-driven conductivity of lizardite-implication to the high conductive layers in craton lithosphere

Junkai Zhang[1,1], Jianguo Du[2,2], and Yanzhang Ma[3,3]

[1]Jilin Normal University
[2]Institute of Earthquake Forecasting, CEA
[3]Texas Tech University

November 30, 2022

Abstract

The electrical transport behavior of lizardite was investigated by *in-situ* impedance measurements up to 22.6 GPa in a diamond anvil cell with comparation to its dehydrated counterpart. The conductivity of lizardite is found to increase one order of magnitude with increasing pressures from 0.2 to 1.9 GPa, due to pressure-activated ionic and electronic transportation. The proton hopping and hopping-created vacancy accounts for the conduction mechanisms. Compression initially promotes proton hopping at lower pressures and then impedes it at elevates pressure to make conduction purely electronic. Compared to the dehydrated specimen, the hydroxyl in lizardite enhances conductivity 4-7 times. The electronic resistivity at higher pressures gradually increases at a constant rate, except in the pressure range where pressure minimized the misfit structural disordering. The pressure-activated proton hopping in the lizardite and other phyllosilicates may ascribe the high conductive layer in the craton lithosphere and geoelectric anomalies related to earthquakes.

Hosted file

`supporting information for public.doc` available at https://authorea.com/users/560979/articles/608715-pressure-driven-conductivity-of-lizardite-implication-to-the-high-conductive-layers-in-craton-lithosphere

Pressure-driven conductivity of lizardite—implication to the high conductive layers in craton lithosphere

Junkai Zhang[a], Jianguo Du[b], Yanzhang Ma[c*]

[a] Key Laboratory of Functional Materials Physics and Chemistry of the Ministry of Education, Jilin Normal University, Siping 136000, P. R. China

[b] United Laboratory of High-Pressure Physics and Earthquake Science, Key Laboratory of Earthquake Prediction, Institute of Earthquake Forecasting, CEA, Beijing 100036, China

[c] Department of Mechanical Engineering, Texas Tech University, Lubbock, TX 79409, USA

*****To whom correspondence should be addressed. E-mail: y.ma@ttu.edu (Y. Ma)

Abstract

The electrical transport behavior of lizardite was investigated by *in-situ* impedance measurements up to 22.6 GPa in a diamond anvil cell with comparation to its dehydrated counterpart. The conductivity of lizardite is found to increase one order of magnitude with increasing pressures from 0.2 to 1.9 GPa, due to pressure-activated ionic and electronic transportation. The proton hopping and hopping-created vacancy accounts for the conduction mechanisms. Compression initially promotes proton hopping at lower pressures and then impedes it at elevates pressure to make conduction purely electronic. Compared to the dehydrated specimen, the hydroxyl in lizardite enhances conductivity 4-7 times. The electronic resistivity at higher pressures gradually increases at a constant rate, except in the pressure range where pressure minimized the misfit structural disordering. The pressure-activated proton hopping in the lizardite and other phyllosilicates may ascribe the high conductive layer in the craton lithosphere and geoelectric anomalies related to earthquakes.

Keywords:

Proton hopping; High conductivity; Ionic transportation; High pressure; Lizardite

1. Introduction

Serpentine enriched in H_2O (~13 wt.%) universally distributes in the crust and upper mantle, and is the primary contributor to the global water cycle in the subduction zone and the hydrothermal alteration of oceanic lithosphere (Schmidt & Poli, 1998; Rüpke et al., 2004). Magnetotelluric survey data reveal pervasive existence of lower resistive zones that are related to the earthquakes in the crust and upper mantle in the continental region (Wei et al., 2001; Xu, 2003; Gürer & Bayrak, 2007; Naganjaneyulu et al., 2013; Yang et al., 2020), subduction zone (Cordell et al., 2019), and throughout the world (Honkura, 1978; Ichiki et al., 2009; Özaydın & Selway, 2020). The lower resistive domains by far are commonly attributed to fluids enrichment. However, the mechanism of electrical transport in the lower resistive domains remains in debating. On the other hand, serpentine dehydration, a common physical performance

of hydrated minerals at high pressure and high temperature, was claimed one of the major causes of intermediate earthquakes (Obara, 2002).

Serpentine belongs to trioctahedral phyllosilicate, with 1:1 stacking of [SiO_4] tetrahedron and [MgO_8] octahedron. The layer curvature and stacking variation lead to three main structural varieties, namely, lizardite with a planar structure, chrysotile with cylindrically rolled layers, and antigorite with periodic reversals of the layer's polarity (Wicks & O'Hanley, 1988). At ambient conditions, serpentine crystallizes in the monoclinic or hexagonal structure (Mellini & Viti, 1994; Capitani & Mellini, 2004). While the crystal structures of serpentine are quite stable, neither amorphization nor other structural phase transition were resolved in natural serpentine up to 10 GPa at zero temperature, only its beta angles (β) were quite largely changed and reversed sign from –0.27° GPa^{-1} to 0.43° GPa^{-1} at 5 GPa (Hilairet et al., 2006).

The hydroxyl OH-groups, being the central focus of present studies, are located at the center of the six-fold tetrahedral ring (inner OH) and between the octahedral and tetrahedral layers (outer OH) (Lemaire et al., 1999) in serpentine. Most studies in the past employed Raman scattering technique to effectively reveal the hydroxyl performance. For instance, a third intense Raman peak between 3730-3770 cm^{-1} was revealed upon compression to 6.7 GPa in lizardite, 8.7 GPa in antigorite, and 2.8 GPa in chrysotile, respectively, in addition to the two common strong OH bands at frequencies range of 3550-3850 cm^{-1} (Auzende et al., 2004; Mizukami et al., 2007). The new peak was ascribed to different origins such as the OH vibrational band with a new mode, the LO modes of the in-phase vibrations associated with stacking disorder or structural defects (Reynard & Wunder, 2006). The result that pressure promotion rate of the outer OH vibrational band elevated slightly at about 6 GPa in contrast to the inner OH vibrational band that had an almost constant promotion rate at all pressure ranges implies the anomalous interaction between the hydrogen ion of the outer OH and neighboring basal oxygen upon compression (Noguchi et al., 2012). This is concordant with the first-principle calculation result of abrupt increase of the OH···O bond angle in outer hydroxyl at 7 GPa (Mookherjee & Stixrude, 2009), and the experimental confirmation (Hilairet et al., 2006).

Measurements of the transportation behavior of a mineral directly reveal its dynamical, electronic, and ionic properties. It would be particularly efficient in characterize the behavior of

hydroxyl in a hydrated mineral. Studies had been conducted with multi-anvil high-pressure apparatuses with particularly focus on revealing the pressure effect on dehydration induced by high temperature (Song et al., 1996) and the relation between the dehydration induced high conductivity and the occurrence of a high-conductivity zone in the lower crust (Zhu et al., 2000). Systematic investigation for the crucial physical behavior of hydroxyl is still lacking. In this work, the recently developed technique of micro-electrical circuit on a diamond anvil facet (Wang et al., 2016) was adopted to *in-situ* measure the impedance spectra of natural lizardite crystal in a diamond anvil cell to explore the transportation properties of its physical excitons (i.e., hydroxyl, proton, and vacancies), in the attempt to investigate the possible connection to high conduction zone at depth of the crust as well as to shallow earthquakes. Synchrotron X-ray diffraction and Raman scattering measurements were also accomplished in revealing the physical mechanism associated with the transportation performance.

2. Experimental description

A natural lizardite sample collected from Xiuyan, northeastern China was adopted in high-pressure measurements. Its chemical composition in comparison with a sample in literature and the theoretical one is given in Table 1. Compared to theoretical composition, our sample is depleted in 1.4 at.% of SiO_2 and 8.1 at.% of MgO while contains 0.55 at.% more FeO and 0.41 at.% F. The concentrations of TiO_2, Al_2O_3, CaO and Na_2O in the detectable components are relatively low compared to those of others (e.g. Tyburczy et al., 1991). The Mg- and Si-sites in the lizardite sample may be slightly substituted with other elements such as Fe, F. The relatively large percentage of F element may be in the substitutional positions of Mg and Si or in the interstitial positions along with other elements. Before measurements, the sample was grinded into fine powder with particle sizes smaller than 5 microns and dried to eliminate effect of adsorbed water. For the comparison, impedance measurements of the dehydrated specimen at 1000 °C (heating rate 20 °C/min) in an atmosphere of nitrogen for 30 minutes (gas flow, 60 ml/min) were performed. The corresponding thermos-gravimetry (TG) traces of the lizardite samples at different heating rate are depicted in Fig. S1 (See Supporting Information).

Table 1. Composition of the experimental sample

	SiO_2/%	TiO_2/%	Al_2O_3/%	FeO/%	MgO/%	MnO/%	CaO/%	Na_2O/%	K_2O/%	F/%	Total/%
Lizardite[a]	42.77	0.02	0.07	0.55	40.11	—	0.01	0.02	—	0.41	83.96
Lizardite[b]	43.36	—	—	—	43.63	—	—	—	—	—	86.99
Lizardite[c]	42.28	0.04	0.42	0.36	41.94	0.08	0.03	0.01	0.02	—	85.18

[a]This study according to the EPMA (Electronic Probe Microanalyzer)

[b]Standardized Molecular Formula ($Mg_3Si_2O_5(OH)_4$)

[c]Tyburczy et al., 1991

A symmetric diamond anvil cell was adopted in the *in-situ* high-pressure measurements. The ruby fluorescence method was used in all high-pressure measurements for the pressure calibration (Mao et al., 1986). In the *in-situ* impedance spectra measurements, an electrode in the insulated platinum parallel-plate configuration was furbished on the flat surface of each of the pair of diamond anvils (Fig. 1). The sample powder was loaded in the sample chamber of a T301 stainless gasket insulated from the anvil electrodes.

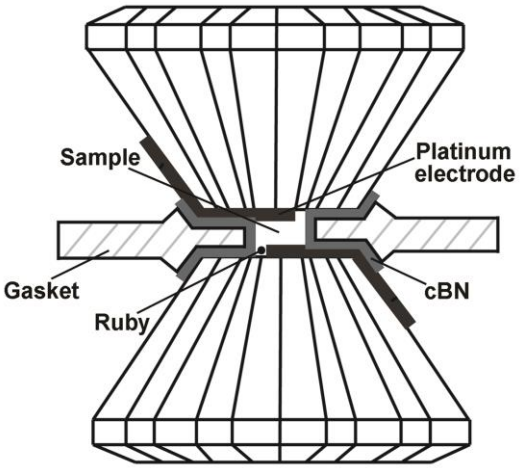

Fig. 1. Electrode configuration in the sample chamber of a diamond anvil cell.

The impedance spectra were measured and recorded using a Solartron 1260 impedance analyzer equipped with a Solartron 1296 dielectric interface from AMETEK Scientific Instruments. At each pressure, an impedance spectrum was measured with the application of the alternative voltage in the time dependent distribution of a sine-function with the magnitude of 1.0 V at alternative frequencies ranging from 0.1 to 10^7 Hz. The spectrum was then processed with the aid of the analytical software Zview2. The equivalent resistance, capacitance, and inductance of the sample were then determined through analyzing the spectrum by the equivalent

circuit method, from which a specific R-C-L circuit was generated depending on the spectrum characteristic.

X-ray diffraction and Raman scattering measurements were also performed at ambient and high pressures for further characterization of the sample as well as for revealing the physical mechanism in the study. Different from the sample loaded for impedance spectrum measurement, silicone oil was employed as pressure transmitting medium in the measurements. The angle dispersive X-ray diffraction measurements were conducted on the beamline 15U1 at Shanghai Synchrotron Radiation Facility with the X-ray wavelength of 6.199 nm. The *in-situ* Raman measurements were performed in a Renishaw InVia system with a 532 nm laser with the maximum output of 200 mW.

3. Results and discussion

The characterization of the samples used in the experiments, the X-ray and Raman measurements to high pressures, as well as the impedance measurements of dehydrated specimen, are first presented and discussed separately for convenient description purpose.

3.1. Sample characterizations and high-pressure studies

3.1.1. X-ray diffraction characterization of the dehydrated sample

X-ray diffraction pattern of the dehydrated specimen for comparison measurements (Fig.2) shows the same patterns of forsterite and enstatite, indicating that the lizardite was dehydrated to transform to forsterite and enstatite. The dehydration process proves to be efficiently removed the hydroxyl components. Therefore, comparison to the resistivity of the dehydrated sample can sufficiently reveal the contribution of the hydroxyl components in the lizardite.

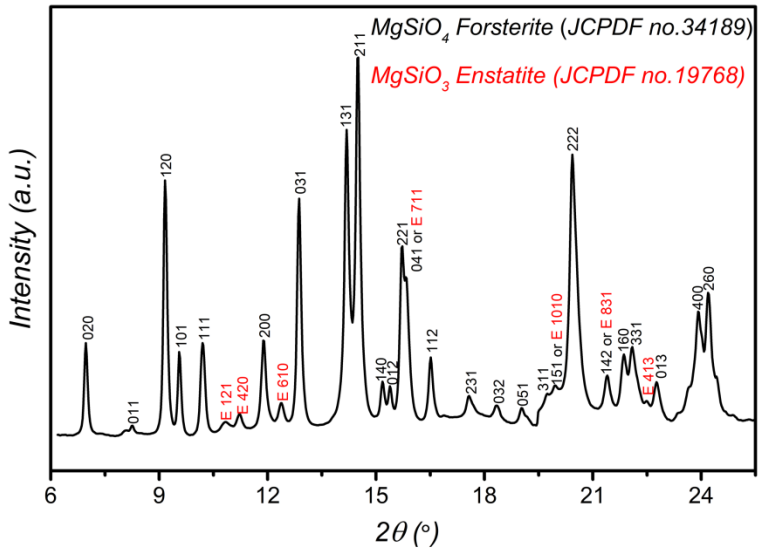

148

149 *Fig. 2. The integrated diffraction pattern of dehydrated specimen at ambient conditions. The*
150 *vertical aligned numbers are Miller indices of the diffraction peaks.*

151 ***3.1.2. X-ray studies at high pressures -- compressibility of lizardite***

152 Selected X-ray diffraction patterns of lizardite under different pressures (inset in Fig. 3) can
153 be indexed to the hexagonal structure with space group: P31m (Auzende, et al., 2004; Hilairet et
154 al., 2006), indicating no structural phase transition occurred at the experimental pressure range.
155 The volume consistently decreased under compression, showing no discontinuity accordingly
156 (Fig. 3). Least square fitting of the volume data to a third-order Birch-Murnaghan equation of
157 state yielded V_0=177.5 (6) Å^3, B_0=69.3 (2) GPa, and B_0'=3.0 (8).

158

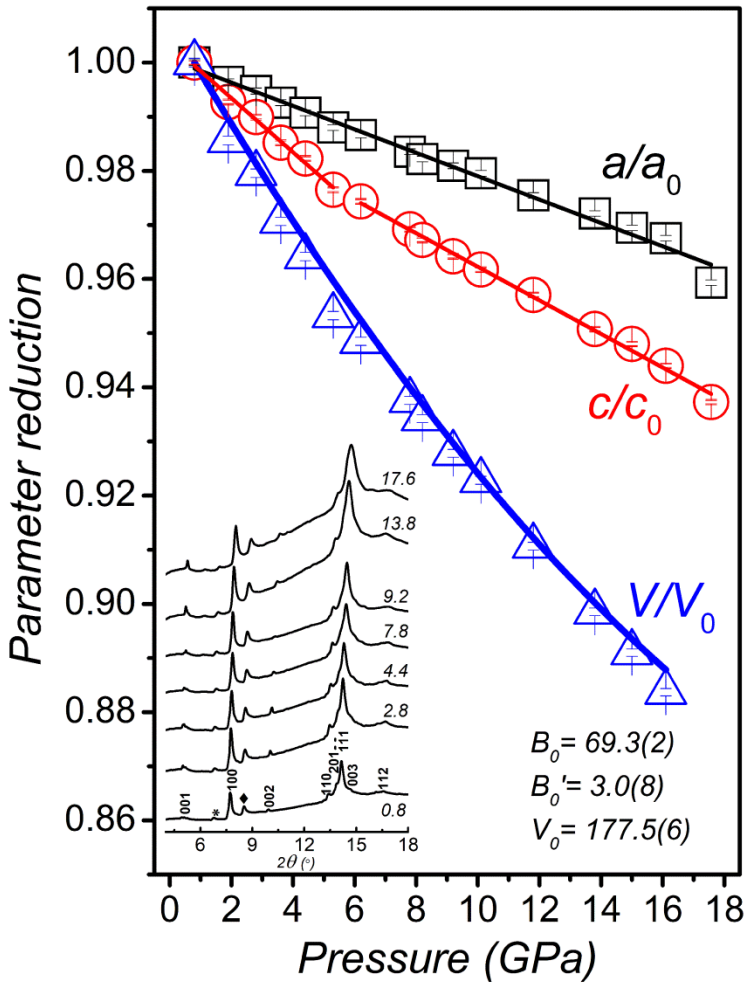

Fig. 3. The pressure dependences of cell parameters and unit cell volume of lizardite. Inset is the integrated diffraction patterns of lizardite at some selected pressures. The number at the right end of the patterns is pressure in GPa; the vertical aligned numbers are Miller indices of the diffraction peak. The peaks marked with star and diamond are from the monoclinic phase in the lizardite mineral.

The axial compressibility showed that the *a*-axis was linearly compressed in the whole pressure range with a rate of 1.7%/GPa except that at 17.6 GPa. It is worth to note that a discontinuity at 5.3 GPa was observed in compressibility along *c*-axis, namely, the slope variated from 3.6% to 2.2%/GPa. Such variation indicated the change of Si-O bond length, which was concordant with that revealed by the Raman measurement (Fig. 4). Compressibility of the *c*-axis was much higher than that of *a*-axis in the whole pressure range even after the transition.

3.1.3 Raman scattering at pressures

The Raman spectra of the lizardite and their pressure dependence at pressures up to 36.9 GPa are shown in Fig. 4 and Fig. 5, respectively. The peaks of 689.4, 377.8, 235.5, 3696.0, and 3663.9 cm^{-1} at 0.2 GPa (the beginning of Raman spectra measurements in DAC) respectively corresponding to modes of Si-O, Mg-OH and Mg-O stretching, and the inner and outer OH stretching were all observed, which are consistent with the previous studies (Lemaire et al., 1999; Auzende et al., 2004; Mizukami et al., 2007). The frequencies of Mg-O stretching mode and Mg-OH stretching mode shifted linearly to the red with the rates of 4.01 and 3.55 cm^{-1}/GPa respectively with pressure elevated up to 36.9 GPa. This reflects the pressure induced strengthening of the MgO and inner OH bonds, which is surprisingly irrelevant to the structural change of lizardite under compression to be discussed below. These two modes were thus utilized as the references for analysis of other modes. The Si-O stretching mode also shifted to the red with increasing pressure with much higher rate of 7.41 cm^{-1}/GPa at the initial compression stage. However, after 5 GPa, the rate was substantially reduced to 2.17 cm^{-1}/GPa, indicating an anomaly of phase structural change at about 5 GPa. In the band of relatively high-frequencies, the inner OH stretching and the outer OH stretching modes also shifted to the red with increasing pressure with the lower rates of 2.55 and 2.05 cm^{-1}/GPa at the initial compression stage, but the rates slightly increased to 3.05 and 2.85 cm^{-1}/GPa when the pressure was higher than 5 GPa. The rate discontinuities of Si-O and outer OH modes indicated the structural deformation.

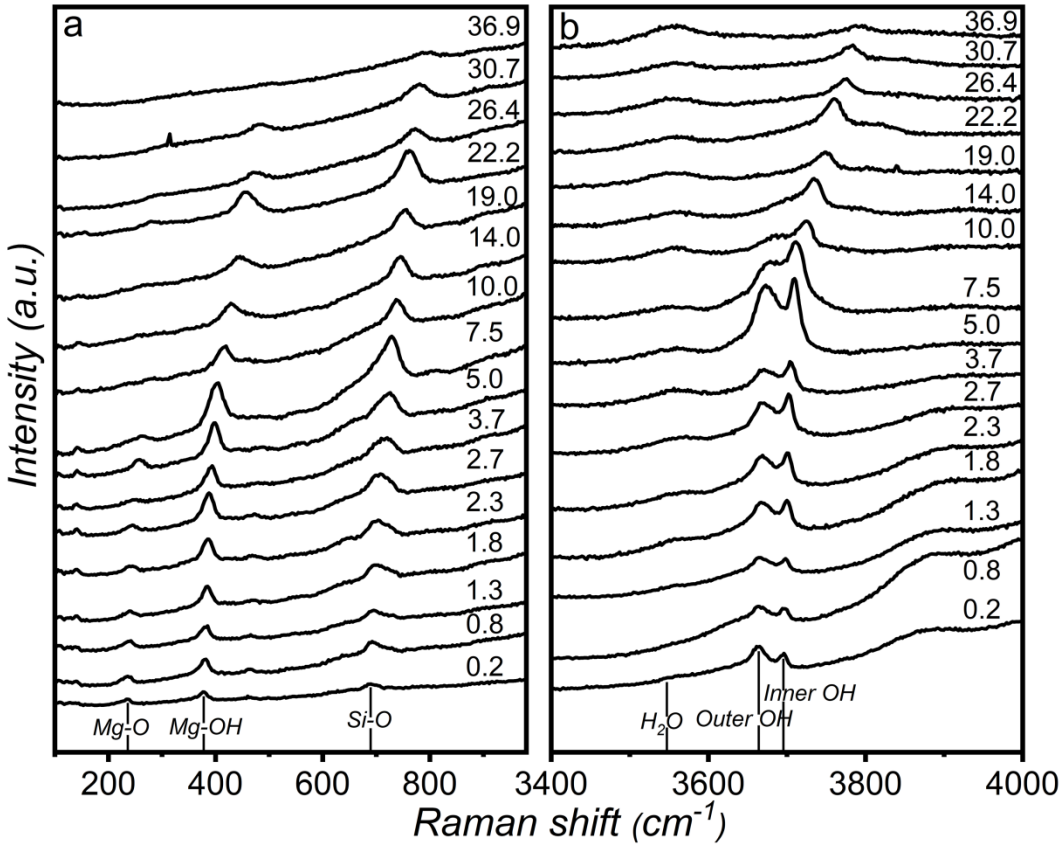

191

192 *Fig. 4. The Raman spectra of lizardite at selected pressures. a), spectra between 100 and 950 cm*

193 *-1 and b), spectra between 3400 and 4000 cm-1. Pressures in GPa are labeled next to the curves.*

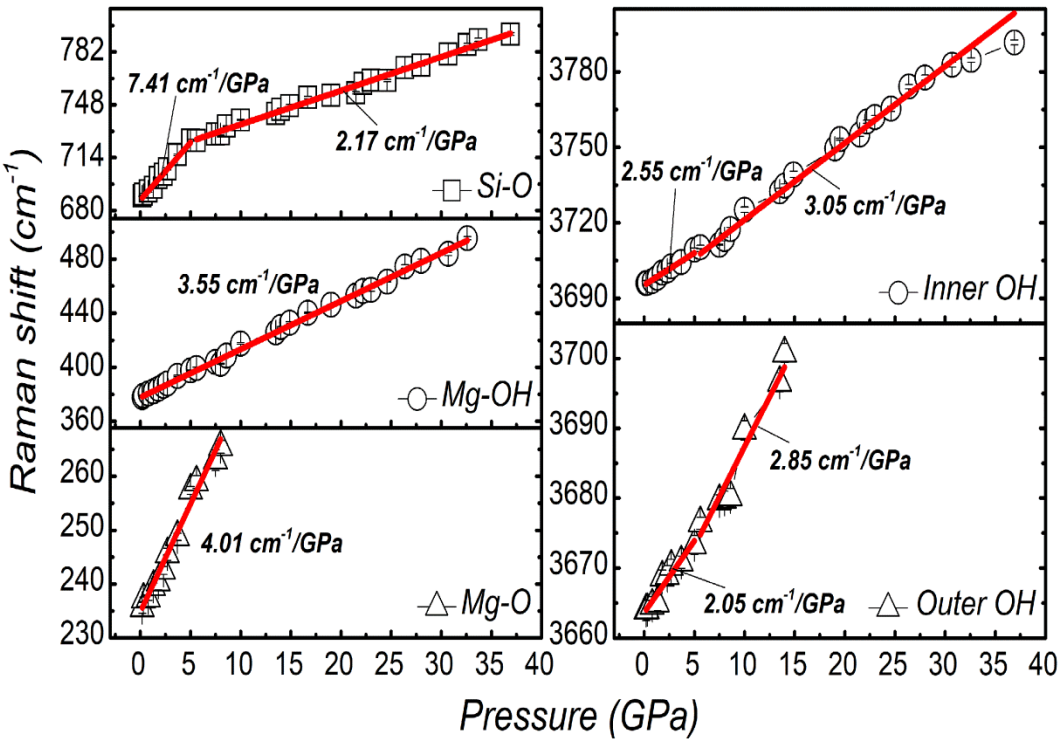

Fig. 5. The pressure dependence of Raman shifts of lizardite. The solid red curves are the linear fitting results. The error bars represent the error generated during the fitting.

3.1.4. Analysis of impedance spectra

The impedance spectra of the natural lizardite and its dehydrated counterpart were respectively measured to 22.1 and 21.8 GPa. The selected impedance spectra in the forms of Nyquist and Bode plots of the lizardite sample (Fig. 6a and Fig. 6c) are compared with those of the dehydrated specimen (Fig. 6b and Fig. 6d).

In the quantitative analysis, an *RC* (resistance-capacitance) equivalent circuit (Fig. 6f) was routinely introduced to simulate the impedance spectra in order to deduce the resistance, capacitance, and the relaxation frequency when the spectra just consist of semicircles. Furthermore, with ascription of the low-frequency straight line to the Debye equivalence, a Warburg element was introduced in addition to an *RC* circuit (Fig. 6e inset), allowing us to retrieve both ionic and electronic resistance (Wang et al., 2016). Comparison between the fitting curves and the measured results (Fig. 6e and 6f) showed a precisely match. Consequently, the electronic and ionic resistances and the relaxation frequencies acquired from the fitting can

precisely reflect the conductive characteristics of the samples.

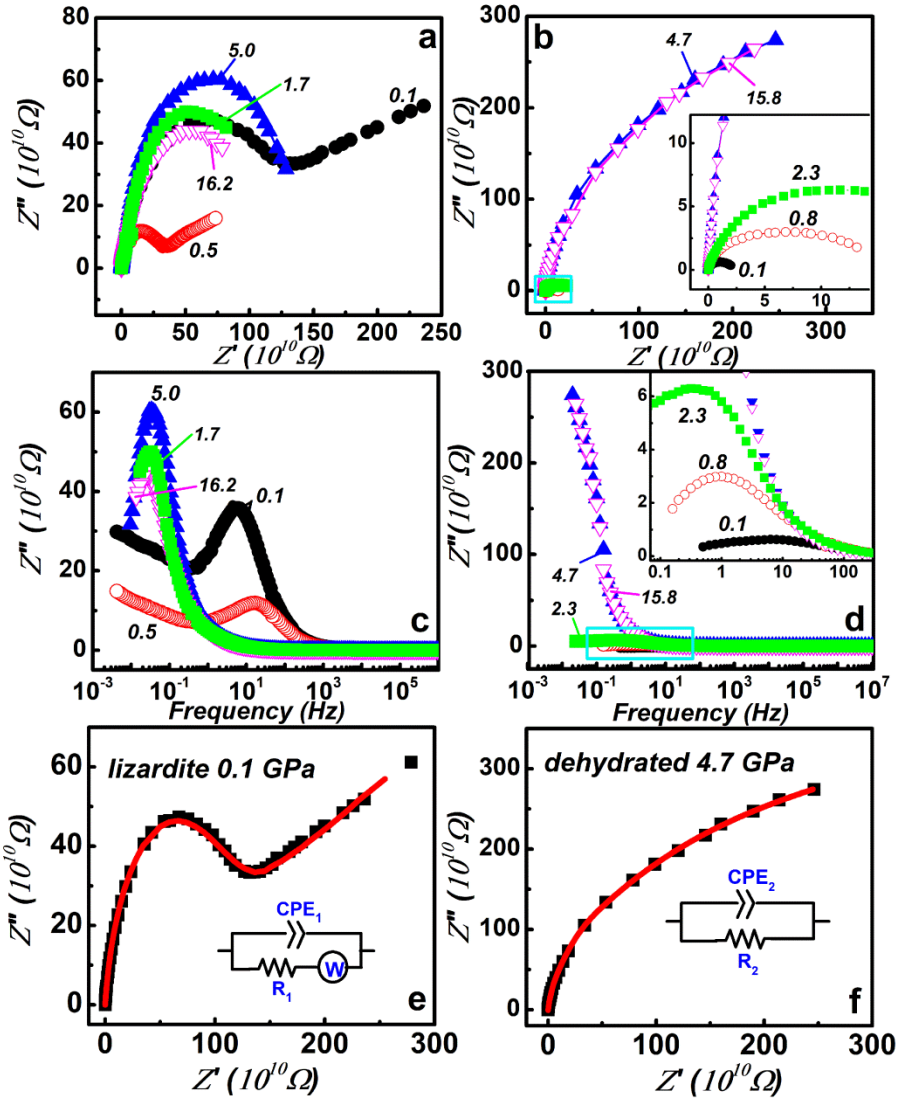

Fig. 6. The Nyquist and Bode plots of the impedance spectra of the lizardite (a and c) and dehydrated sample (b and d) and examples of their simulation to a Debye equivalent circuit (e, R_1, electronic resistance, CPE_1, double-layer capacitance on the sample-electrode interfaces, W, Warburg impedance), and to an RC equivalent circuit (f, R_2, electronic resistance, CPE_2, double-layer capacitance on the sample-electrode interfaces). Numbers labeled next to the curves (a to d) are pressures in GPa.

3.1.5. The conduction of dehydrated specimen

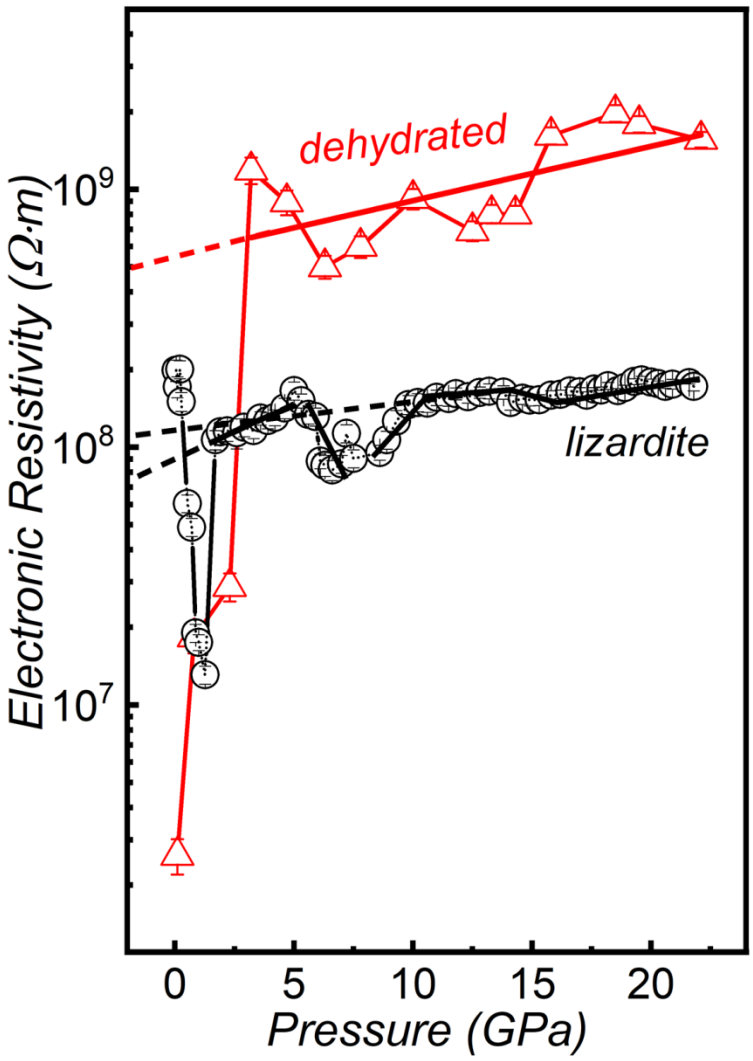

Fig. 7. The electronic resistivity of lizardite in comparison with that of dehydrated specimen. OH, resistivity reduction due to hydration. MF, resistivity due to octahedral and tetrahedral misfit.

Commonly in a crystalline substance, the conduction may be caused by the exciton either from the crystallized grain or from crystalline interface. The bonding strength (bonding energy) for similar type of excitons may variate because of atomic distance difference between the atoms at grain boundary from those in the crystal, resulting in different resistivity and relaxation frequencies. In the impedance spectra of both the natural lizardite and the dehydrated specimen, just one semi-circle occurred under the experimental pressures. The commonly observed double-semi-circle spectrum, representing the conductivity of grain interior and grain boundary in a

powdered crystalline material, was not observed. This is an indication that there is only one type of detectable charge carrier in the electronic conduction. The heating dehydration process in preparation of the specimen caused high concentration of imperfections. A majority of them would be in the form of vacancy, of which interface to the crystalline framework served as exciton, i.e., the charge carriers. The high concentration of such excitons contributed to the conduction and substantially lowered resistivity of the specimen, resulting in the lower resistivity than that of the lizardite sample at very low pressures (Fig. 7). The electronic resistivity of the lizardite and the dehydrated specimen was respectively 1.9×10^{8} and 2.6×10^{6} Ω·m near ambient pressure. At higher pressures, the conductivity of dehydrated specimen was about 2 orders of magnitude higher than that of the lizardite sample. With pressure elevation, the vacancy shrank and was eventually closed, causing the sharply reduction of exciton concentration at above 4 GPa, eventually indistinguishable from those excitons in the crystalline frameworks. The geophysical significance of the vacancy-introducing exceptional high conductivity and vacancy-closing dumped conductivity at the pressures will be discussed further.

The magnitude of resistivity of dehydrated specimen remained at the order of 10^{9} Ω·m above 3.2 GPa, showing a general trend of gently positive slop (Fig.7). Extrapolation of the fitting line at high pressure to room pressure yielded a resistivity of about 4.9×10^{8} Ω·m. This is in good approximation of the electrical response of the magnesium silicate networks of the dehydrated sample without the vacancy effect. The resistive values of dehydrated specimen were generally ~4 to 7 times higher than those of the lizardite. The phenomenon, which seems incongruous to the common sense that hydration of a mineral would favor higher conductivity, indicates that the dominant electronic conduction of lizardite isn't likely originated from the magnesium silicate polyhedron frameworks. Therefore, the conductivity of lizardite can be dictated by the hydroxyl in its structure.

3.2. Conductivity of lizardite

3.2.1. Reversals of ionic and electronic conductivity -- the proton hopping below 1.9 GPa

The pressure driven conduction reversals (Fig. 8) illustrate variations of the resistivity and relaxation frequency of lizardite with pressure increase (<3 GPa). The conductive mechanism of lizardite exhibited both electronic and ionic characters near ambient pressure, and the values of

electronic and ionic resistivity were 1.9×10^{8} and 2.8×10^{7} Ω·m, respectively. The values decreased with increasing pressure up to 1.3 GPa, and interestingly attained the lowest value of 1.3×10^{7} Ω·m near 1.3 GPa, but thereafter increased with increasing pressure. The ionic conduction was inhibited after increasing pressure larger than 1.9 GPa, while the electronic resistivity continuously increased thereafter. Therefore, it is clear that 1.9 GPa is the critical pressure of ionic conduction inhibition. Correspondingly, the relaxation frequency of the lizardite sample was in the order of 10 Hz at ambient conditions, mildly increased linearly with increasing pressure to 1.3 GPa, but then abruptly dropped two orders of magnitude to the order of 0.01 Hz at 1.9 GPa. At pressures above 1.9 GPa, the relaxation frequency continuously decreased at a lower rate until completely out of the instrumentation observation limit.

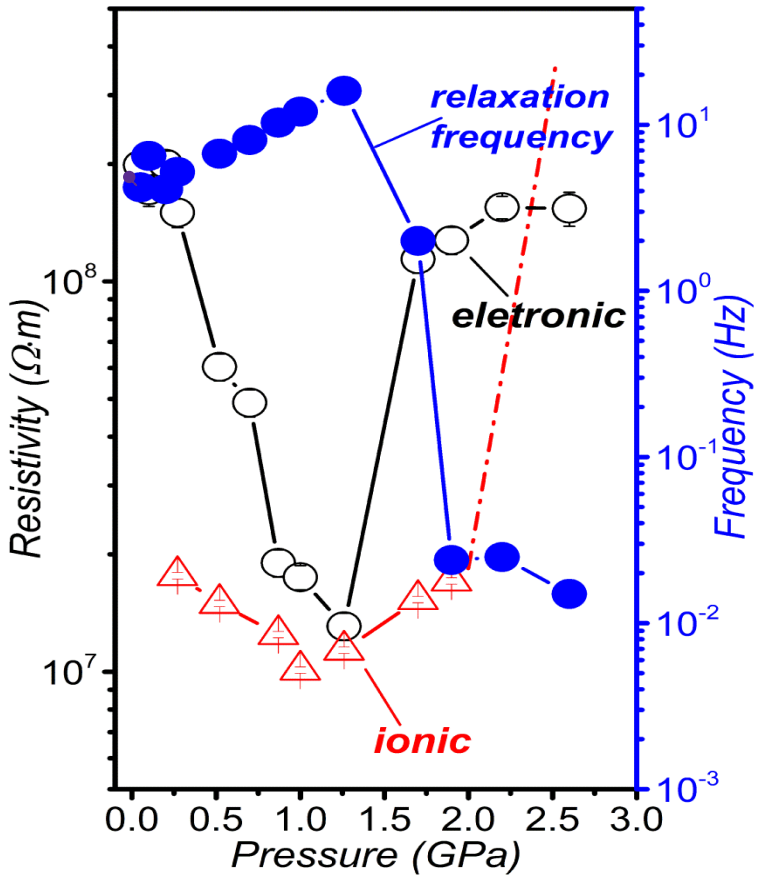

Fig. 8. The ionic and electronic resistivity and relaxation frequency of lizardite below 2.6 GPa.

The proton hopping -- The hydrogen proton is an important carrier in hydrated minerals except for vacancies that produced positive (hole) and negative (electron) charges. The ionic conductivity of the natural lizardite at 0-1.9 GPa indicated that transportation of ion potentially

was by the protons and vacancies. As aforementioned, the comparable conductive experiment of the dehydrated specimen has eliminated the possibility that the detected ionic conduction was induced by the vacancies in the [SiO_4] tetrahedral and [MgO_8] octahedral frameworks. The much lower conductivity of the natural lizardite, therefore, proved that the hydroxyl interior dominated the conductivity behavior. Consequentially, the proton hopping was proposed as the mechanism of the ionic conductivity at the pressures of 0-1.9 GPa. More specifically, there are two different proton locations in lizardite crystalline. One, the so-called inner proton H(4), is located on a three-fold rotational axis with crystallographic coordinate of (0, 0, z), a position in the center among three Si-O tetrahedra, which is similar to the proton positions in talc (Mookherjee & Stixrude, 2009). The protons in such positions were restricted its delocalization, instead, those protons remained in the so-called form of O(4)H(4) hydroxyl and didn't contribute to the observed ionic transportation. The other one, the so-called inter-plane proton H(3), situates between the Mg-O octahedral and Si-O tetrahedral layers, a gap sheltered by a layer of octahedra sheet and an opposite tetrahedra sheet. The proton locates in the gap outside the oxygen-planes in the octahedral side at the coordinate of (x, 0, z). Thus, there is a layer of protons in the lizardite crystal. Theoretical calculation indicated that the length of the bond formed between this kind of proton and the oxygen [O(3)] was above 0.097, and closed to 0.098 nm at pressures between 0-7 GPa (Mookherjee & Stixrude, 2009), which approximated those in liquid water. Thus, the minimal bond stretching compared to that in gaseous state (0.096 nm) indicated that the hydroxyl protons forms weak bond between the hydrogen and the non-bridge oxygen in the tetrahedra plane. The distance between the neighbor oxygen planes formed by octahedra and tetrahedra (the width of the gap) was far more than double the O(3)H(3) bond lengths at all experimental pressures. Such a large opening space provided the essential room for proton hopping. Therefore, the hopping of H(3) proton from one site to another mainly caused the low ionic conduction of lizardite at the lower pressures.

At the pressures below 3.2 GPa, the H(3)-proton transported along the tunnel between Mg-O and Si-O polyhedrons, serving as a positive charge carrier, accounting for the low-pressure ionic conduction (Fig. 8). Simultaneously, the proton run-away produced the proton vacancies that formed the negative charge carriers, contributing to the electrical conduction. Initial pressure elevation served as eliminating lattice and atomic vibrations, which reduced the scattering to both ionic and electronic charge carriers and increased their free-transportation-distance,

resulting in the reduction of resistivity till 1.3 GPa. The pressure elevation simultaneously enhanced the interaction between the proton-created vacancy and the Mg-O octahedron. Since the relaxation frequency is proportional to the square root of holding force over mass of vibron, the relaxation frequency of the natural lizardite increased with initial pressure increase (Fig.8). However, further pressure elevation above 1.3 GPa reduced the gap between the Si-O and Mg-O polyhedrons and enhanced the interaction between the charge carriers and the Si-O tetrahedron. Such additional interaction impeded and eventually hindered the proton hopping so that the ionic resistivity was promoted and consequentially the electronic resistivity was promoted. At the same time, the relaxation frequency abruptly reduced because of increasing mass of exciton, resulting in the reversal from proton hopping introduced vacancy to the eventual hydroxyl. At pressures above 1.9 GPa, the gap was severely narrowed so that the proton migration became inhibited and the hydroxyl exciton worked as the main electronic charge carrier.

3.2.2. Gap reduction inducing proton localized oscillation and polyhedral misfit

The transition of the effective charge carrier from vacancy type to hydroxyl dipole type controlled the resistivity of lizardite. The effective electronic conduction charge carrier alternated from vacancy types to the hydroxyl dipole type in the natural lizardite when the pressure induced proton localization was completed. Specifically increasing pressure above 1.9 GPa, the localized O(3)H(3) and its interaction with the environment regulated the electronic conductivity of lizardite. Due to O(3)H(3) was located in the gap between Mg- and Si-polyhedrons, the electronic behavior exceedingly correlated with the structural features at the pressures. The high-pressure electrical characteristics, in turn, responded to the structural variation of lizardite crystalline to compression (Fig. 3).

The electronic resistivity elevated exponentially one order of magnitude to 10^8 Ω·m when pressure was increased from 1.3 to 2.0 GPa (Fig. 7), which was attributed to the transition of the effective charge carrier from vacancy type to hydroxyl dipole type. Then pressure increased to 5 GPa, the resistivity gradually increased. However, the resistivity decreased rapidly from 5 to 11 GPa (the maximum reduction reached 20% at around 7 GPa), which was caused by another resistivity reversal. After then, the resistivity increased with pressure elevation with a rate similar to that from 2 to 5 GPa.

The gap narrowing affected the resistivity under compression. The mild pressure promotion of resistivity in the pressure range of 2-5 and above 15 GPa was directly related to the gap narrowing. The pressure coefficient of resistivity was proportional to the crystal lattice's *c*-axial reduction. The rate of the crystal lattice's *c*-axial reduction indicated that the gap became narrowed much faster than other directions (Fig. 3), introducing stronger interaction between hydroxyl and tetrahedral framework. With the minimal hydrogen bond of O(3)H(3) itself (showing no change under compression (Mookherjee & Stixrude, 2009)), the pressure induced stronger interaction between the hydroxyl O(3)H(3) and the Mg-octahedron as well as the Si-tetrahedron, which refrained hydroxyl from transportation and resulted in higher resistivity. This is supported by the outer O(3)H(3) stretching mode of the higher pressure strengthening rate below 5 GPa (Fig. 4 and Fig. 5).

Another factor is so-called expansion of the Si-tetrahedra. The octahedra and tetrahedra in serpentine showed quite different compressibility [Auzende et al., 2004; Nestola et al., 2009]. At medium pressure range (below 7 GPa), the Si-O stretching mode in our Raman spectra (Fig.4) showed a softening around 5 GPa, providing an evidence of such an expansion. The expansion of tetrahedra framework can be considered as providing larger scattering cross-section to charge transportation that elevated electronic resistivity of the natural lizardite.

The polyhedral misfit affected the resistivity. The resistivity reversal in 5-11 GPa (Fig.7) was caused by the pressure-driven misfit between the octahedral and tetrahedral layers in the lizardite. In fact, the non-negligible misfit effect contributed to resistivity performance as well as gap reduction at all pressures above 1.9 GPa. Such misfit mutually altered the interaction between hydroxyl against polyhedron of the gap, introducing extra scattering to the charge carrier and consequentially additional resistance. The resistivity ramped up to the maximum at about 5 GPa and then dropped steeply to a valley minimized at 7 GPa (Fig. 7). Furthermore, the misfit started to increase from the 7 GPa valley to attain another peak point at 20 GPa. Similarly, the theoretical calculation indicated that polyhedral misfit attained the maximum at about 5 GPa and then dropped to a valley at 7 GPa (Mookherjee & Stixrude, 2009). The resistivity diagram showed continuous increase with the pressure elevation up to 20 GPa, further substantiating the correlation between the misfit and resistivity, e.g., the higher the misfit in lizardite, the higher the resistivity. The plot (Fig. 9) demonstrates the effect of polyhedral misfit on the resistivity.

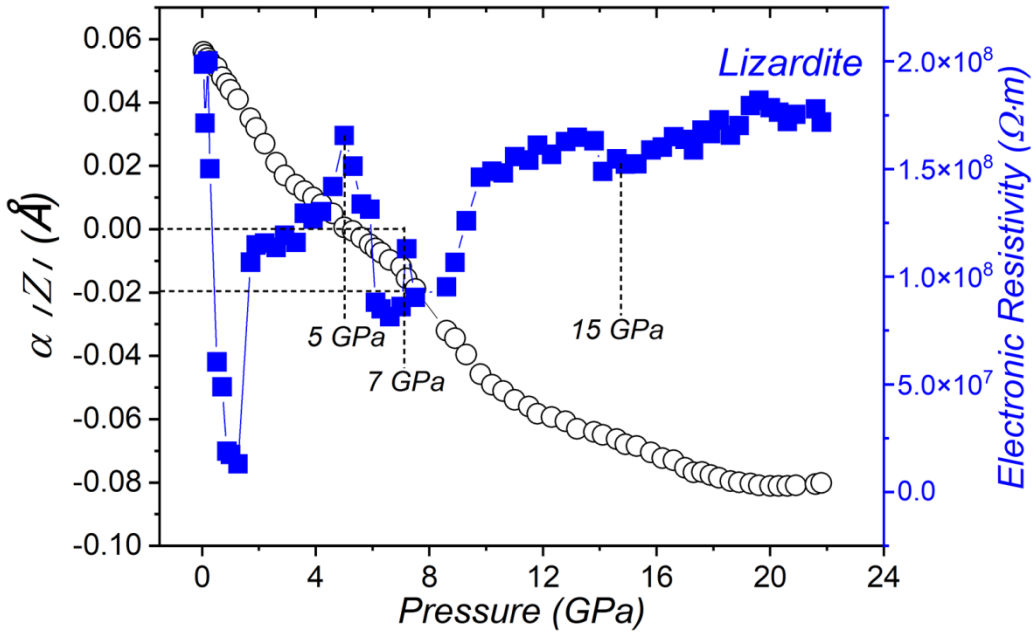

363

364 *Fig. 9. The pressure dependence of the misfit between the octahedral and tetrahedral layers*
365 *(denoted by αZ) and the electronic resistivity of lizardite. α shows evolution of the tetrahedral*
366 *angle. The misfit between the tetrahedral layer and octahedral layer is depicted by the oxygen*
367 *lattice corrugation, $\Delta z=[zO_{max}-zO_{min}]\times c$, where zO is the z crystallographic coordinate of the*
368 *basal O atom.*

369 The observed resistivity curve drift at 15 GPa was caused by the structural reorganization
370 that was reported by Mookherjee and Stixrude (2009). The average length of Si-O bond, the
371 hydrogen bond angle and volume of tetrahedron likely exhibited discontinuities in the structural
372 change of the serpentine framework. Whereas, it should be pointed out that both gap narrowing
373 and polyhedral misfit were direct response to compressibility and the resistive peak at about 5
374 GPa was the compressibility introduced without regarding to a phase transformation.

375 ## 4. Geological significance

376 The high conductive layers in the Earth are usually attributed to geofluids and melt. The
377 lower electrical resistance of a geological domain can be caused by many factors such as
378 dehydration of hydrated minerals (Song et al., 1996; Dobson et al., 2002; Ichiki et al., 2009; Hu
379 et al., 2018), connected conductive minerals or fluids in rock pores (Wei et al., 2001; Xu, 2003;
380 Cordell et al., 2019; Yang et al., 2020), loading of stress (Naganjaneyulu et al., 2013) and/or

seismic waves (Grib et al., 2019). However, it is impossible that the well-connected pore fluids widely distribute in the lower crust and upper mantle. The observed phenomenon of lowest resistivity at ~1.3 GPa proves that the mineral hydration in the lithosphere commonly elevates the overall conductivity at least by one order of magnitude. The existence of large domain of such minerals may itself form a high conductive layer at depths between 30~50 km. Therefore, the observed high pressure activated high conductivity, particularly the proton hopping introduced ionic and electronic conductivity may be considered as genetic mechanism of the high conductive layers at least in the craton lithosphere in which geothermal gradient is lower, i.e., the pressure promotion of high conductivity of the lizardite and other hydrated phyllosilicates up to 1.9 GPa may contribute to the high conductive layer in the craton lithosphere of up to ~60 km depth in the Earth. In addition, serpentine can form well-connected net in the alterated basic and altrabasic rocks that distribute universally in the lithosphere. Since the vast area of hydrated minerals, they as dominant domain as well as miner trace filler between other nonconducting minerals can extend high conductive region to form a high conductive layer as observed. This resolves the concerns of conductive connections between conductive phases in models such as the one where the conductive anomalies in both upper and lower lithospheric mantle in the cratonic regions was proposed likely caused by the existence of well-connected minor phases associated with metasomatic fluids and hydration in the upper mantle and well-connected minor conducting phases at lower mantle (Özaydın & Selway, 2020).

The existence of the hydrated minerals in the lithosphere is considered to be related the lower resistive layers (Hu et al., 2018; Özaydın & Selway, 2020), which are related to earthquakes (Xu, 2003; Gürer & Bayrak, 2007; Ichiki et al., 2009; Abdul Azeez et al., 2018). Correlation between seismic and electromagnetic data indicated that conductivity linearly depended on the shear and bulk moduli in craton lithospheric rocks (Jones et al., 2009). Our experimental result of the resistivity change with pressure, therefore, provides new data for understanding the genetic mechanism of the seismic geoelectric anomalies and high conductive layers in the continental lithosphere, especially in the region of lacking connected-pores in the lower lithosphere. Particularly, under the certain conditions such as presence of electric magnetic field interruption and accumulation of stress in a process of earthquake, protons in hydrated phyllosilicates may escape from the network of crystalline minerals to form free charge, resulting in seismic electrical anomalies. Thus, the loosely held (pressure activated) protons in hydrated

phyllosilicates can become the resource of electrical charge, which may account for the observed electric anomalies before, during, and after earthquakes described in Gürer & Bayrak, 2007.

5. Conclusion

The study of the electrical transportation of lizardite and dehydrated specimen in correlation with X-ray and Raman results shows that the structural hydroxyl induces one extra order of magnitude in conductivity. The conductivity was dominantly dependence of gap formed between the Mg-O and Si-O frames. The pressure induced narrowing of such gap promoted the resistivity linearly. Pressure-activated ionic transportation in lizardite, induced by proton hopping, was found at pressures below 1.9 GPa. The moderate compression drives the formation of proton in lizardite, in which both additional ionic and electronic excitons were induced, resulting in one order of magnitude elevation in both ionic and electronic conductivity. The pressure-activated proton hopping is most likely the genetic mechanism of the high conductive layers in the craton lithosphere and geoelectric anomalies related to earthquakes.

Acknowledgement

This work was supported by the National Natural Science Foundation of China (Grant Nos. 11904128) and the United Laboratory of High-pressure Physics and Earthquake Science. Synchrotron X-ray experiments were performed at Shanghai Synchrotron Radiation Facility. EPMA (Electronic Probe Microanalyzer) was performed at China Earthquake Administration. The authors thank Dr. Lei Liu for experimental technical support.

Data Availability Statement

The data sets for the misfit between the octahedral and tetrahedral layers are provided in Mookherjee and Stixrude (2009); and the other data sets processed by Jilin Normal University and China Earthquake Administration are available at a general repository, Zenodo, http://doi.org/10.5281/zenodo.4595783.

References

Abdul Azeez, K. K., Mohan, K., Veeraswamy, K., Rastogi, B. K., Gupta, A. K., & Harinarayan, T., (2018). 3D crustal resistivity structure beneath the Wagad after shock zone of the 2001 Bhuj earthquake, Kutch, India: Heterogeneous resistivity structure controlled by widespread fluid infiltration and clues to aftershocks pattern. *Tectonophysics*, *747-748*, 54-67. https://doi.org/10.1016/j.tecto.2018.09.014

Auzende, A. L., Daniel, I., Reynard, B., Lemaire, C., & Guyot, F. (2004). High-pressure behaviour of serpentine minerals: a Raman spectroscopic study. *Physics and Chemistry of Minerals*, *31*, 269-277. https://doi.org/10.1007/s00269-004-0384-0

Capitani, G., & Mellini, M. (2004). The modulated crystal structure of Antigorite: the m=17 polysome. *American Mineralogist*, *89*, 147-158. https:// doi.org/10.2138/am-2004-0117

Cordell, D., Unsworth, M. J., Diaz, D., Reyes-Wagner, V., Currie, C. A., & Hicks, S. P. (2019). Fluid and melt pathways in the central Chilean subduction zone near the 2010 Maule earthquake (35°-36° S) as inferred from magnetotelluric data. *Geochemistry, Geophysics, Geosystems*, *20*, 1818-1835. https://doi.org/10.1029/2018GC008167

Dobson, D. P., Meredith, P. G., & Boon, S. A. (2002). Simulation of subduction zone seismicity by dehydration of serpentine. *Science*, *298*, 1407-1410. https://doi.org/10.1126/science.1075390

Grib, N. N., Uzbekov, A. N., Imaev, V. S., Grib, G. V., & Abetov, A. E. (2019). Variations in the geoelectric properties of the rock masses as a result of the seismic effects of industrial explosions. *IOP Conf. Series: Earth and Environmental Science*, *362*, 012120. https://doi.org/10.1088/1755-1315/362/1/012120

Gürer, A., & Bayrak, M. (2007). Relation between electrical resistivity and earthquake generation in the crust of West Anatolia, Turkey. *Tectonophysics*, *445*, 49-65. https://doi.org/10.1016/j.tecto.2007.06.009

Hilairet, N., Daniel, I., & Reynard, B. (2006). P-V equation of state and relative stabilities of serpentine varieties. *Physics and Chemistry of Minerals*, *33*, 629-637.

https://doi.org/10.1007/s00269-006-0111-0

Honkura, Y. (1978). Electrical conductivity anomalies in the earth. *Geophysical Surveys*, *3*, 225-253. https://doi.org/10.1007/bf01449555

Hu, H., Dai, L., Li, H., Sun, W., & Li, B. (2018). Effect of dehydrogenation on the electrical conductivity of Fe-bearing amphibole: Implications for high conductivity anomalies in subduction zones and continental crust. *Earth and Planetary Science Letters*, *498*, 27-37. https://doi.org/10.1016/j.epsl.2018.06.003

Ichiki, M., Baba, K., Toh, H., & Fuji-ta, K. (2009). An overview of electrical conductivity structures of the crust and upper mantle beneath the northwestern Pacific, the Japanese Islands, and continental East Asia. *Gondwana Research*, *16*, 545-562. https://doi.org/10.1016/j.gr.2009.04.007

Jones, A. G., Evans, R. L, Eaton, & D. W. (2009). Velocity-conductivity relationships for mantle mineral assemblages in Archean cratonic lithosphere based on a review of laboratory data and Hashin–Shtrikman extremal bounds. *Lithos*, *109*, 131-143. https://doi.org/10.1016/j.lithos.2008.10.014

Lemaire, C., Guyot, F., & Reynard, B. (1999). Vibrational spectroscopy (IR and Raman) of OH groups in chrysotile, lizardite and antigorite. *European Union of Geosciences* 10. Strasbourg, pp. 654.

Mao, H. K., Xu, J., & Bell, P. M. (1986). Calibration of the ruby pressure gauge to 800 kbar under quasi-hydrostatic conditions. *Journal of Geophysical Research: Solid Earth*, *91*, 4763-4767. https://doi.org/10.1029/JB091iB05p04673

Mellini M., & Viti, C. (1994). Crystal structure of Lizardite-1T from Elba, Italy. *American Mineralogist*, *79*, 1194-1198. https://doi.org/10.1029/94JB01129

Mizukami, T., Kagi, H., Wallis, S. R., & Fukura, S. (2007). Pressure-induced change in compressional behavior of the O-H bond in chrysotile: a Raman high-pressure study up to 4.5 GPa. *American Mineralogist*, *92*, 1456-1463. https://doi.org/10.2138/am.2007.2489

Mookherjee, M., & Stixrude, L. (2009). Structure and elasticity of serpentine at high-pressure. *Earth and Planetary Science Letters*, *279*, 11-19. https://doi.org/10.1016/j.epsl.2008.12.018

Naganjaneyulu, K., Aggarwal, L., & Santosh, M. (2013). Magnetotelluric studies in the Central India Tectonic Zone: Implications for intraplate stress regimes and generation of shallow earthquakes. *Journal of Asian Earth Sciences*, *78*, 318-326. https://doi.org/10.1016/j.jseaes.2013.07.012

Nestola, F., Angel, R. J., Zhao, J., Garrido, C. J., Sánchez-Vizcaíno, V. L., Capitani, G. C., & Mellini, M. (2009). Antigorite equation of state and anomalous softening at 6 GPa: an in situ single-crystal X-ray diffraction study. *Contributions to Mineralogy and Petrology*, *160*, 33-43. https://doi.org/10.1007/s00410-009-0463-9

Noguchi, N., Moriwaki, T., Ikemoto, U., & Shinoda, K. (2012). OH group behavior and pressure-induced amorphization of antigorite examined under high pressure and temperature using synchrotron infrared spectroscopy. *American Mineralogist*, *97*, 134-142. https://doi.org/10.2138/am.2012.3904

Obara, K. (2002). Nonvolcanic deep tremor associated with subduction in southwest Japan. *Science*, *296*, 1679-1681. https://doi.org/10.1126/science.1070378

Özaydıın, S., & Selway, K. (2020). MATE: An analysis tool for the interpretation of magnetotelluric models of the mantle. *Geochemistry*, *Geophysics*, *Geosystems*, 21. https://doi.org/10.1029/2020gc009126

Reynard, B., & Wunder, B. (2006). High-pressure behavior of synthetic antigorite in the MgO-SiO_2-H_2O system from Raman spectroscopy. *American Mineralogist*, *91*, 459-462. https://doi.org/10.1038/1781472a0

Rüpke, L. H., Morgan, J. P., Hort, M., & Connolly, J. A. D. (2004). Serpentine and the subduction zone water cycle. *Earth and Planetary Science Letters*, *223*, 17-34. https://doi.org/10.1016/j.epsl.2004.04.018

Schmidt, M., & Poli, S. (1998). Experimentally based water budgets for dehydrating slabs and consequences for arc magma generation. *Earth and Planetary Science Letters*, *163*, 361-379. https://doi.org/10.1016/S0012-821X(98)00142-3

Solum, J. G., Hickman, S. H., Lockner, D. A., Moore, D. E., van der Pluijm, B. A., Schleicher, A. M., & Evans, J. P. (2006). Mineralogical characterization of protolith and fault rocks from the SAFOD main hole. *Geophysical Research Letters*, *33*, L21314-1-5. https://doi.org/10.1029/2006GL027285

Song, M. S., Xie, H. S., Zhang, Y. M., Xu, Y. S., Guo, J., Xu, Z. M., & Xu, H. G. (1996). Dehydration temperature of serpentine at elevated temperatures and pressures by electrical conductivity method and its implication. *Acta mineralogical sinica*, *16*, 178-183. https://doi.org/10.1007/BF02843354

Tyburczy, J. A., Duffy, T. S., Ahrens, T. J., & Lange, M. A. (1991). Shock wave equation of state of serpentine to 150 GPa: Implications for the occurrence of water in the Earth's lower mantle. *Journal of Geophysical Research: Solid Earth*, *96*B, 18011-18027. https://doi.org/10.1029/91JB01573

Ulmer, P., & Trommsdorff, V. (1995). Serpentine stability to mantle depths and subduction-related magmatism. *Science*, *268*, 858-861. https://doi.org/10.1126/science.268.5212.858

Wang, Q. L., Liu, C. L., Han, Y. H., Gao, C. X., & Ma, Y. Z. (2016). The determination of ionic transport properties at high pressures in a diamond anvil cell. *Review of Scientific Instruments*, *87*, 123904. https://doi.org/10.1063/1.4971304

Wei, W., Unsworth, M., Jones, A., Booker, J., Tan, H., Nelson, D., Chen, L., Li, S., Solon, K., Bedrosian, P., Jin, S., Deng, M., Ledo, J., Kay, D., & Roberts, B. (2001). Detection of widespread fluids in the Tibetan crust by magnetotelluric studies. *Science*, *292*, 716-718. https://doi.org/10.1126/science.1010580

Wicks, F. J., & O'Hanley, D. (1988). Serpentine minerals: structure and petrology. In: Bailey SW (ed) Hydrous phyllosilicates. *Reviews in Mineralogy* (vol. 19, pp. 91-167). Washington DC: Mineralogical Society of America.

Xu C. (2003). The cause of formation of the upper mantle and crust high conductive layers in Chinese mainland and the study of Tangshan Earthquake. *Earth Science Frontiers*, *10*(Suppl), 101-111. https://doi.org/10.3321/j.issn:1005-2321.2003.z1.016

Yang, W., Jin, S., Zhang, L., Qu, C., Hu, X., Wei, W., Yu, C., & Yu, P. (2020). The three-

546 dimensional resistivity structures of the lithosphere beneath the Qinghai-Tibet plateau.
547 *Chinese Journal of Geophysics*, *63*, 817-827. https://doi.org/10.6038/cjg2020N0197

548 Zhu, M. X., Xie, H. S., Guo, J., Bai, W. M., & Xu, Z. M. (2001). Impedance spectroscopy
549 analysis on electrical properties of serpentine at high pressure and high temperature. *Science*
550 *in China* (Seris D), *44*, 336-345. https://doi.org/10.1007/BF02907104

551 Zoback, M., Hickman, S., & Ellsworth, W. (2010). Scientific drilling into the San Andreas fault
552 zone. *Eos, Transactions American Geophysical Union*, *91*, 197-199.
553 https://doi.org/10.1029/2010EO220001

554

Figure 1.

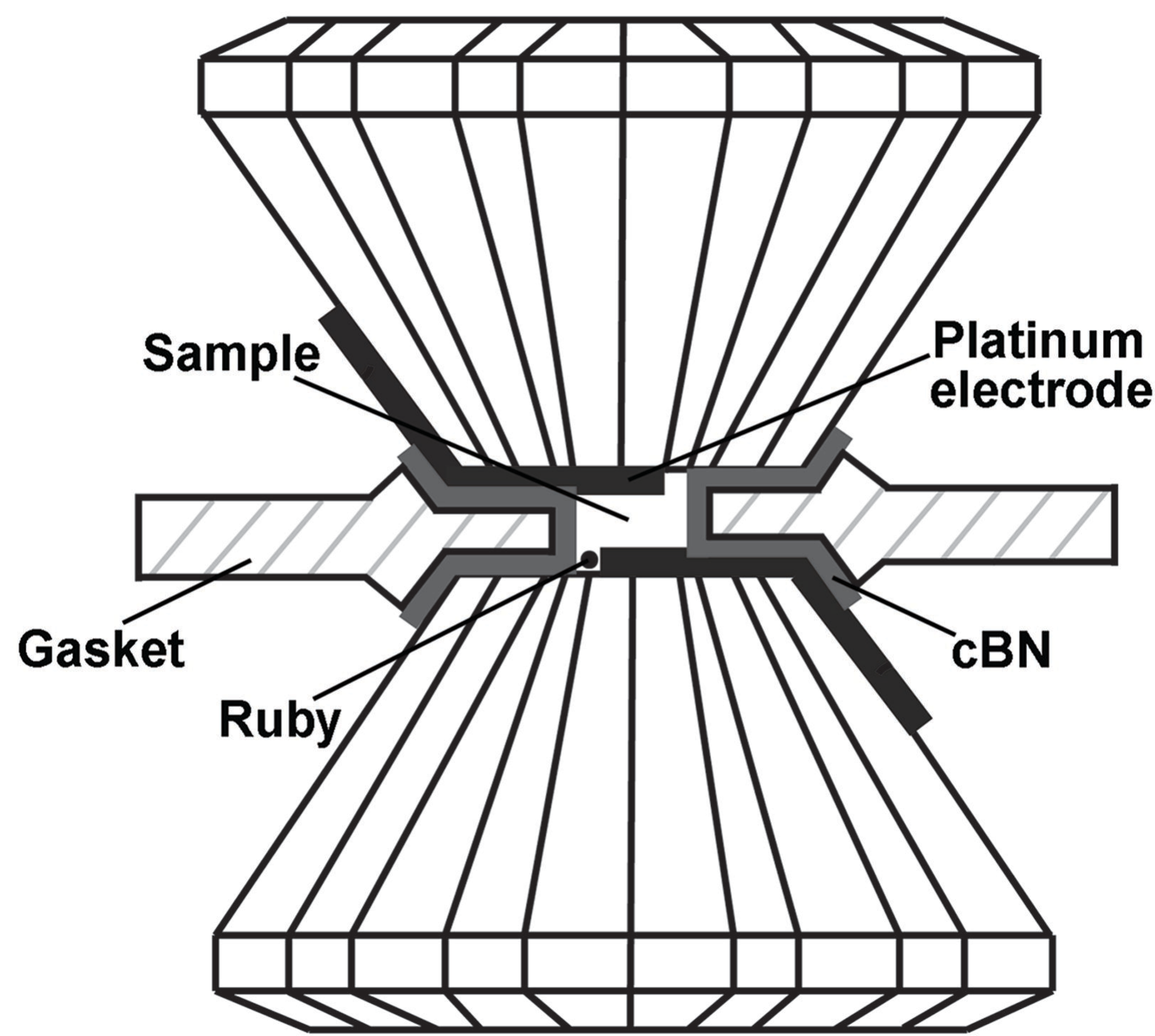
Sample
Platinum electrode
Gasket
cBN
Ruby

Figure 2.

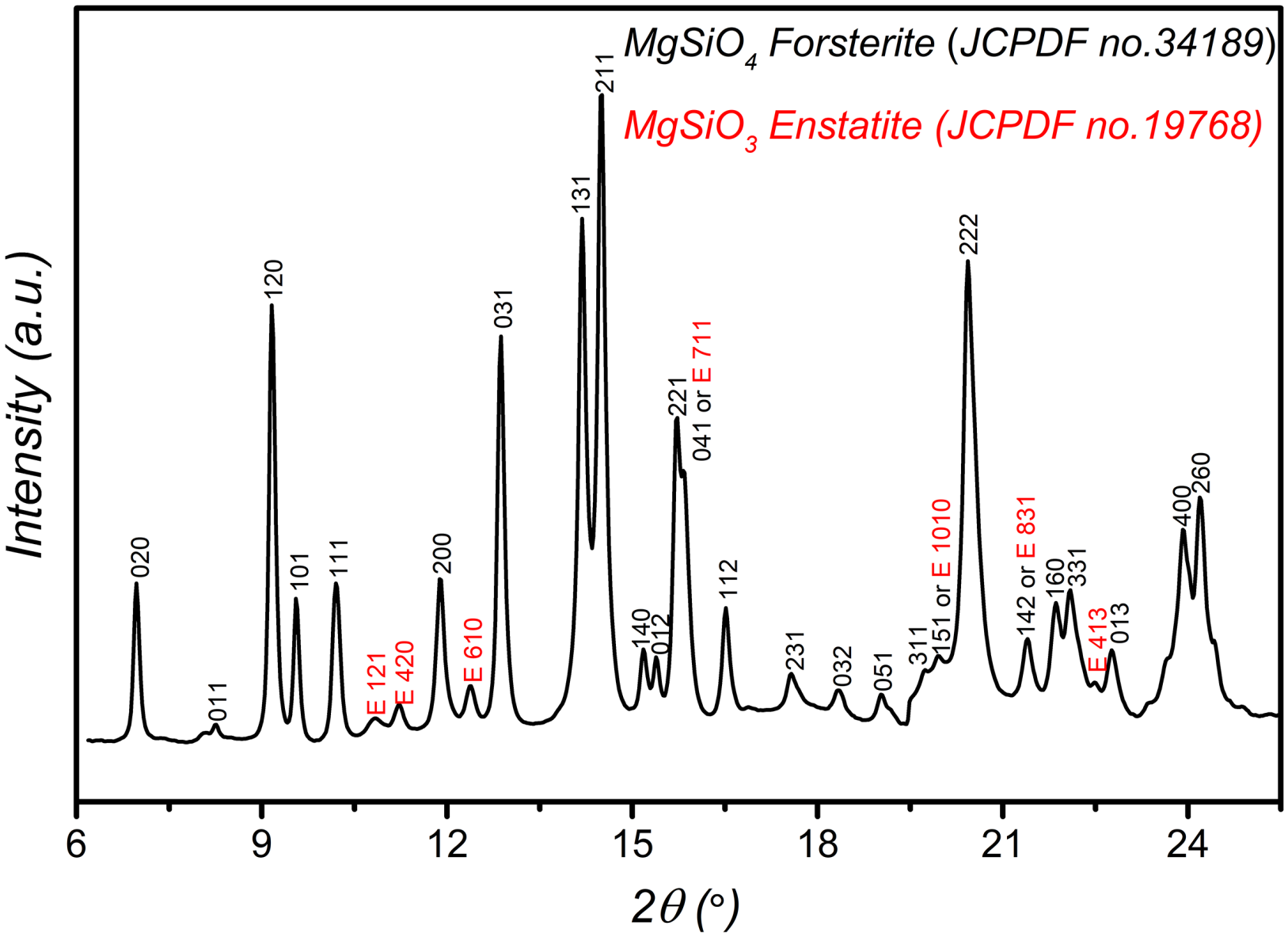
MgSiO4 Forsterite (JCPDF no.34189)
MgSiO3 Enstatite (JCPDF no.19768)
Intensity (a.u.)
2θ (°)
020
011
120
101
111
E 121
E 420
200
E 610
031
131
211
140
012
221
041 or E 711
112
231
032
051
311
151 or E 1010
222
142 or E 831
160
331
E 413
013
400
260
6
9
12
15
18
21
24

Figure 3.

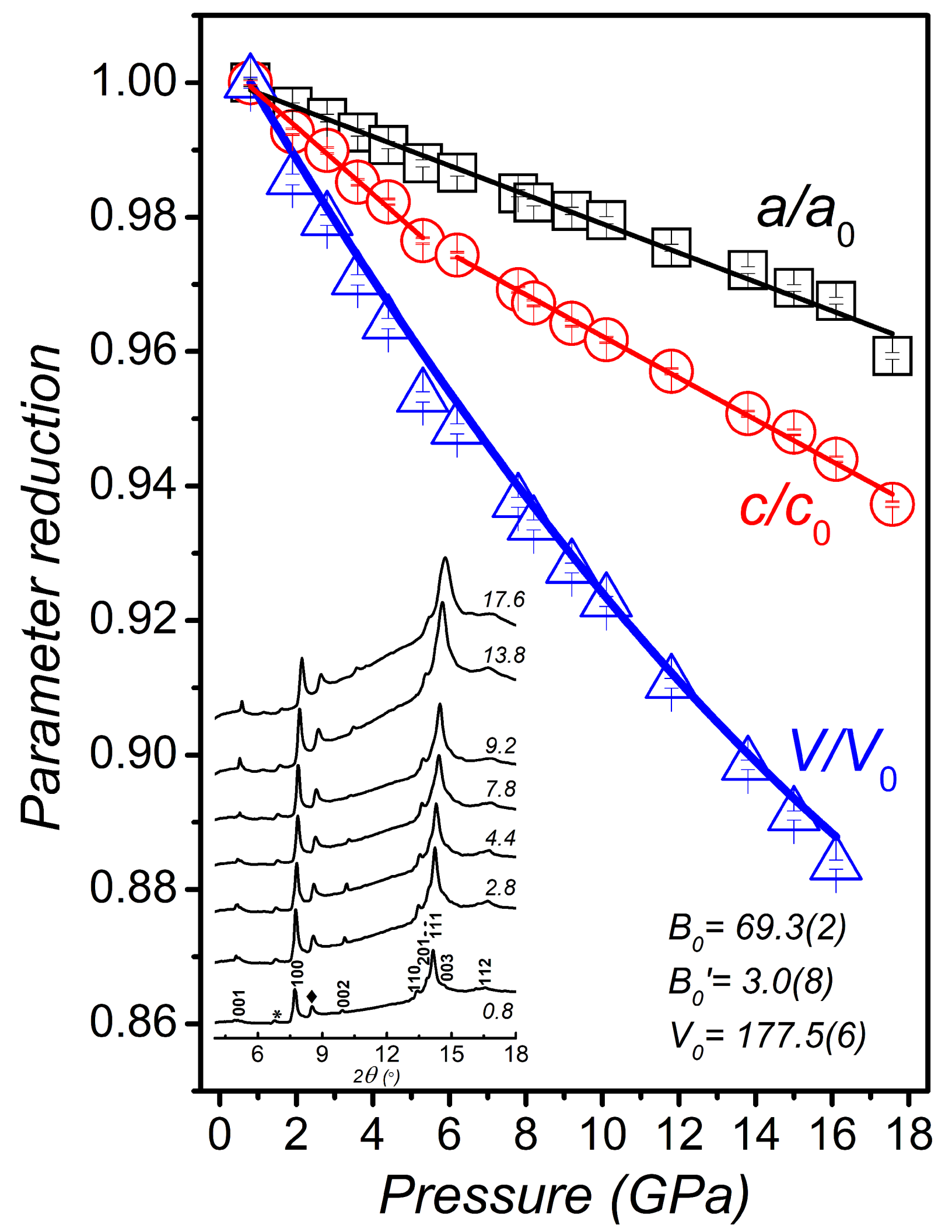
Parameter reduction
Pressure (GPa)
a/a0
c/c0
V/V0
B0= 69.3(2)
B0'= 3.0(8)
V0= 177.5(6)
17.6
13.8
9.2
7.8
4.4
2.8
0.8
001
100
002
110
201
111
003
112
2θ (°)

Figure 4.

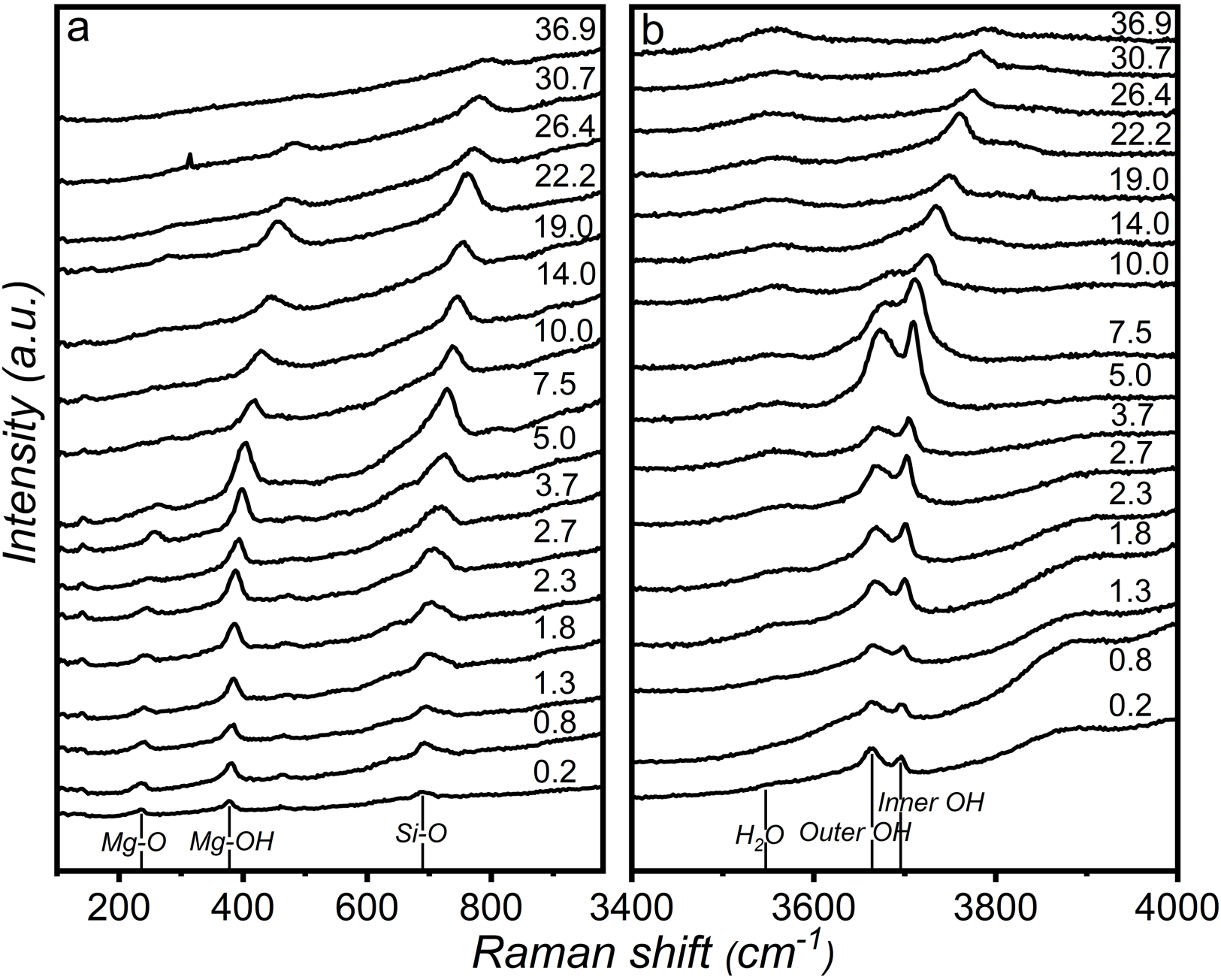
a
b
36.9
30.7
26.4
22.2
19.0
14.0
10.0
7.5
5.0
3.7
2.7
2.3
1.8
1.3
0.8
0.2
Mg-O
Mg-OH
Si-O
H2O
Outer OH
Inner OH
Intensity (a.u.)
200
400
600
800
3400
3600
3800
4000
Raman shift (cm-1)

Figure 5.

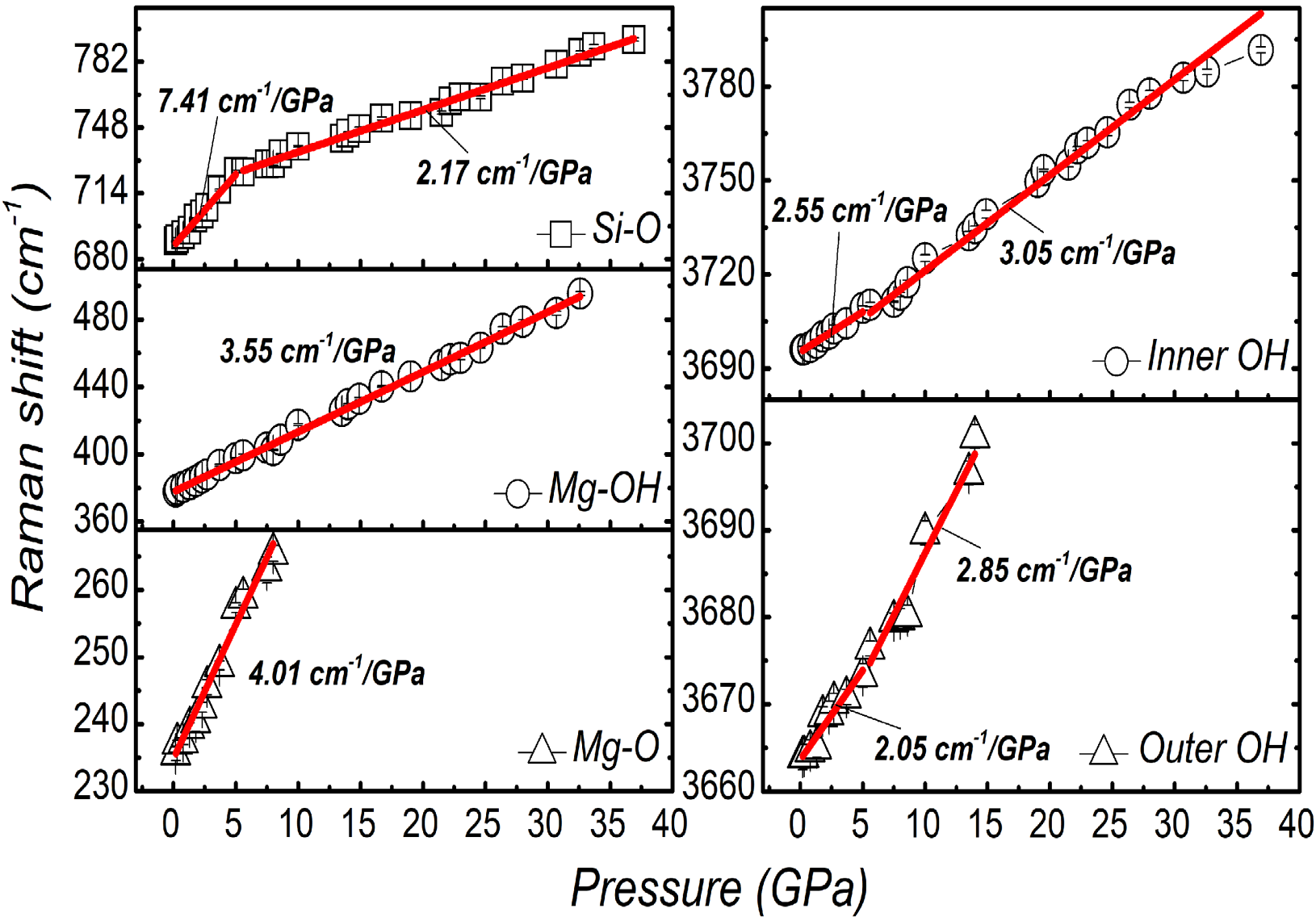
Raman shift (cm-1)
Pressure (GPa)
7.41 cm-1/GPa
2.17 cm-1/GPa
Si-O
3.55 cm-1/GPa
Mg-OH
4.01 cm-1/GPa
Mg-O
2.55 cm-1/GPa
3.05 cm-1/GPa
Inner OH
2.85 cm-1/GPa
2.05 cm-1/GPa
Outer OH

Figure 6.

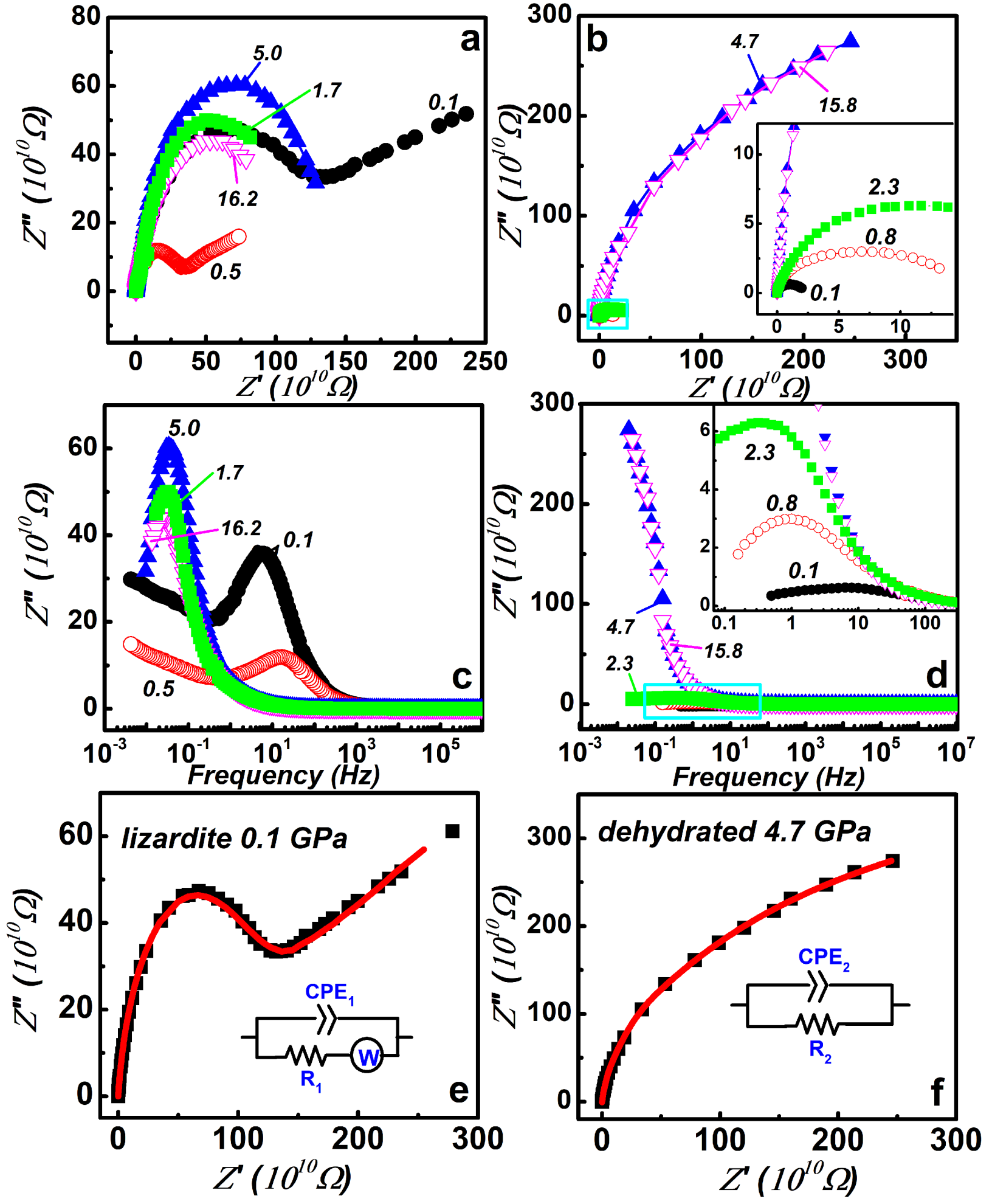
a
5.0
1.7
0.1
16.2
0.5
Z'' (10^10 Ω)
Z' (10^10 Ω)
b
4.7
15.8
2.3
0.8
0.1
c
5.0
1.7
16.2
0.1
0.5
Frequency (Hz)
d
2.3
0.8
0.1
4.7
15.8
2.3
lizardite 0.1 GPa
CPE1
R1
W
e
dehydrated 4.7 GPa
CPE2
R2
f

Figure 7.

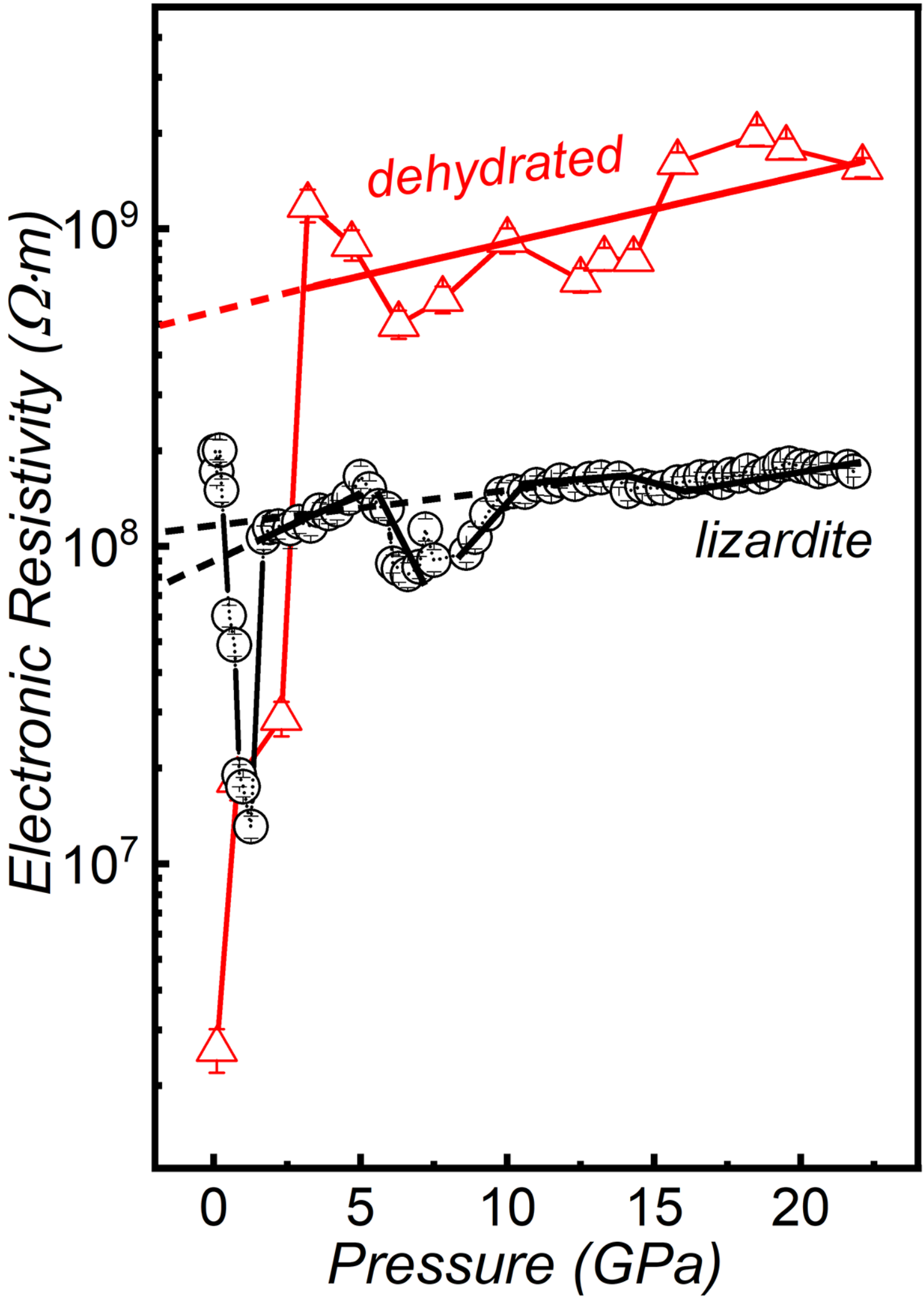
dehydrated
lizardite
Electronic Resistivity (Ω·m)
10^9
10^8
10^7
0
5
10
15
20
Pressure (GPa)

Figure 8.

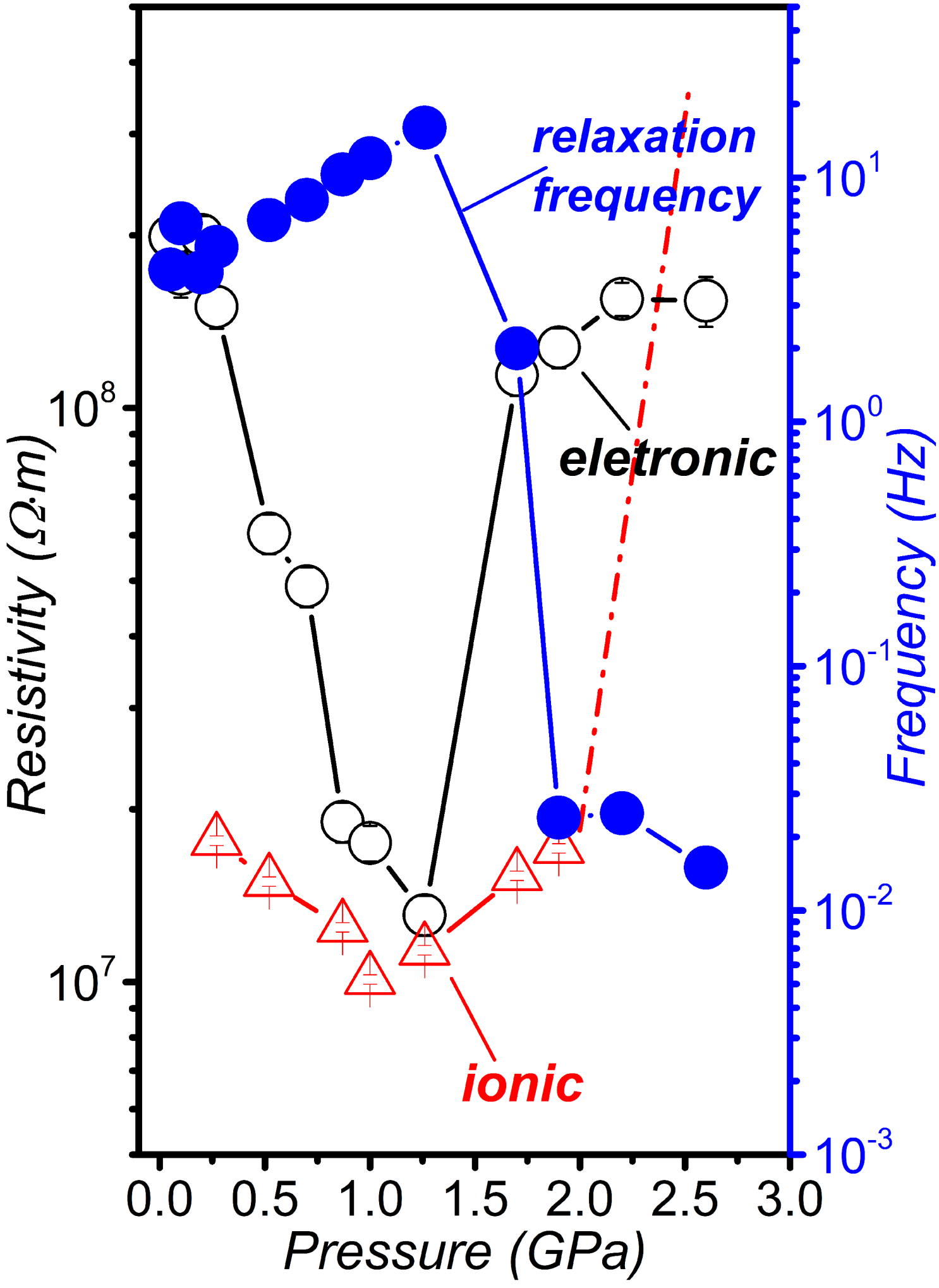
relaxation
frequency
eletronic
ionic
Resistivity (Ω·m)
Frequency (Hz)
Pressure (GPa)
10^8
10^7
10^1
10^0
10^-1
10^-2
10^-3
0.0
0.5
1.0
1.5
2.0
2.5
3.0

Figure 9.

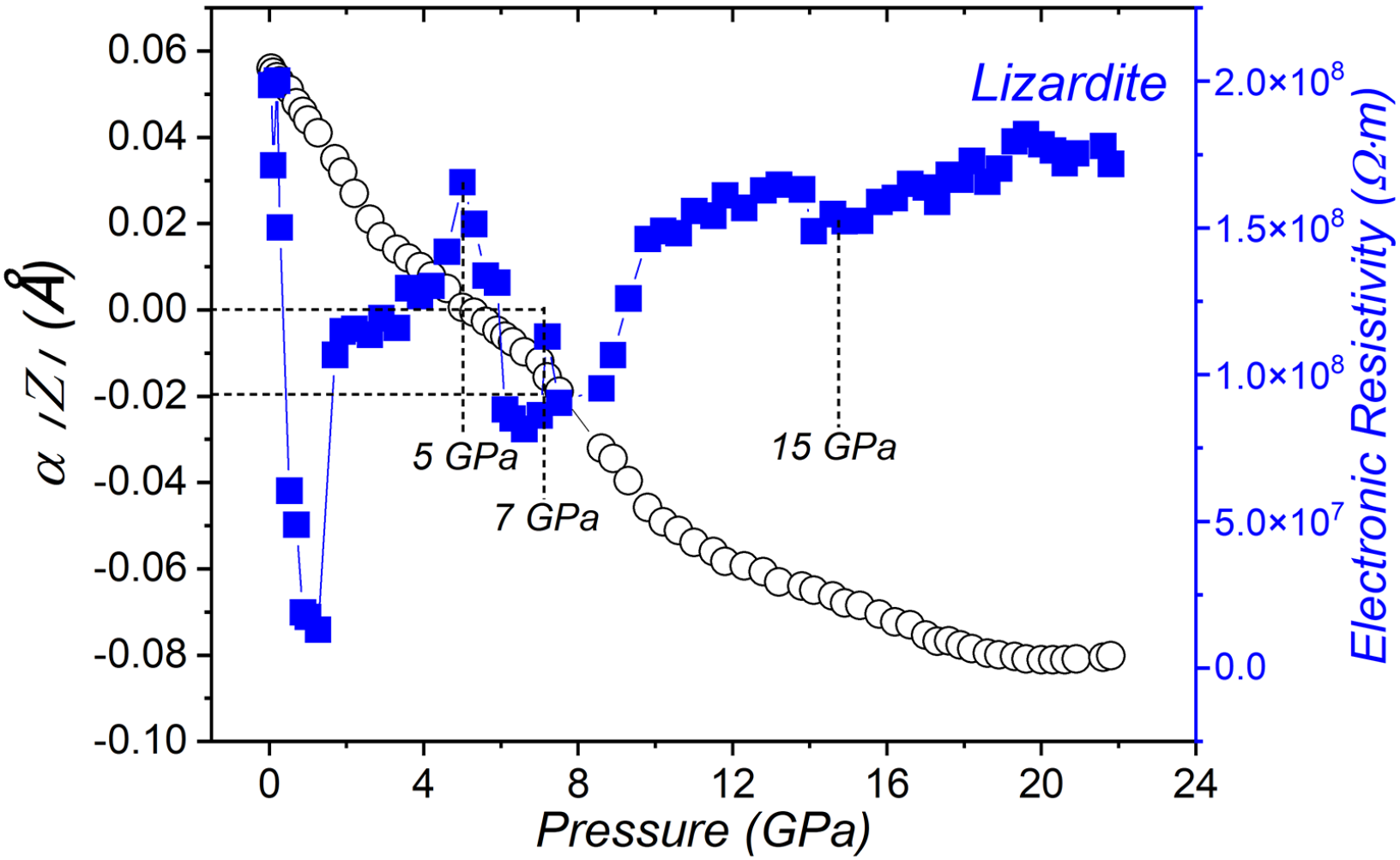
Lizardite
5 GPa
7 GPa
15 GPa
Pressure (GPa)
Electronic Resistivity (Ω·m)
0.06
0.04
0.02
0.00
-0.02
-0.04
-0.06
-0.08
-0.10
0
4
8
12
16
20
24
2.0×10^8
1.5×10^8
1.0×10^8
5.0×10^7
0.0